

# Reduced-order Koopman modeling and predictive control of nonlinear processes

Xuewen Zhang<sup>a</sup>, Minghao Han<sup>a</sup>, Xunyuan Yin<sup>a,\*</sup>

<sup>a</sup>School of Chemistry, Chemical Engineering and Biotechnology, Nanyang Technological University, 62 Nanyang Drive, 637459, Singapore

## Abstract

In this paper, we propose an efficient data-driven predictive control approach for general nonlinear processes based on a reduced-order Koopman operator. A Kalman-based sparse identification of nonlinear dynamics method is employed to select lifting functions for Koopman identification. The selected lifting functions are used to project the original nonlinear state-space into a higher-dimensional linear function space, in which Koopman-based linear models can be constructed for the underlying nonlinear process. To curb the significant increase in the dimensionality of the resulting full-order Koopman models caused by the use of lifting functions, we propose a reduced-order Koopman modeling approach based on proper orthogonal decomposition. A computationally efficient linear robust predictive control scheme is established based on the reduced-order Koopman model. A case study on a benchmark chemical process is conducted to illustrate the effectiveness of the proposed method. Comprehensive comparisons are conducted to demonstrate the advantage of the proposed method.

**Keywords:** Data-driven control, Koopman operator, model order reduction, model predictive control, nonlinear process.

## 1 Introduction

Complex industrial processes have been commonly adopted across various industries due to their potential to offer better operating safety, operational efficiency, production consistency, and product quality [1–3]. To attain these advantages, it is crucial to implement cost-effective advanced process control to appropriately regulate the process operation in real-time. However, the large scales and high nonlinearity of modern industrial processes present challenges in the development and implementation of scalable advanced control schemes [4, 5].

---

\*Corresponding author: X. Yin. Tel: (+65) 6316 8746. Email: xunyuan.yin@ntu.edu.sg.

The development of a successful advanced control system requires a high-fidelity model that is capable of accurately representing the dynamical behavior of the underlying industrial process. If sufficient physics information is available for establishing nonlinear first-principles models to predict the process dynamics, then nonlinear model predictive control (MPC) represents a widely recognized solution to the control of nonlinear processes. In the context of process control, various nonlinear MPC algorithms and approaches have been proposed for nonlinear processes [6–10]. However, when the process scale increases with more tightly interconnected physical units being integrated, it becomes overwhelmingly challenging to derive differential equations to accurately characterize their dynamics [11]. Therefore, the applications of the above-mentioned nonlinear MPC approaches to large and complex industrial processes are still limited. Additionally, even if a first-principles nonlinear model is accessible, the online implementation of these nonlinear MPC algorithms can be demanding. Specifically, the production capacity scales up along with the increase in the number of key states and input variables, which leads to more expensive computation in solving larger-scale (constrained) nonlinear optimization [12]. In this work, we aim to address the two limitations of nonlinear system by developing a more efficient approach to control large-scale nonlinear processes. We propose to establish a data-driven linear model to account for nonlinear process dynamics and exploit linear MPC to account for optimal nonlinear process operations.

The Koopman theory [13] provides a promising framework for building linear models in a lifted state-space to predict the dynamical behaviors of nonlinear systems/processes [14–18]. An exact Koopman operator can be challenging to be established, and may have infinite dimensions. Therefore, the direct application of Koopman theory to real-world nonlinear processes for simulations and monitoring/decision-making has been impractical. This has motivated the exploration of a finite-dimensional approximation of the exact Koopman operator, and powerful data-driven approximation methods were proposed [17–19]. These approximation methods have greatly facilitated the development of data-driven linear control schemes for general nonlinear systems [15,18,20]. In [15,18], Koopman operators were used as linear predictors of nonlinear dynamics, and linear MPC was developed to control nonlinear processes. In [21], a hybrid Koopman MPC framework consisting of multiple Koopman models and local controllers was proposed to manage the operation of a pulping process that exhibits differing dynamics. In [22], the Lyapunov-based MPC framework has been exploited to ensure the closed-loop stability of Koopman-based MPC. Additionally, in [22,23], the Lyapunov function has also been included as one of the lifting functions that map the original nonlinear state-space to a lifted linear state-space for Koopman modeling. To account

for the model mismatch between a Koopman operator and the actual dynamics of the underlying nonlinear system, robust Koopman MPC methods were proposed [20, 24]. Offset-free MPC [25, 26] has been integrated with Koopman-based modeling to mitigate the impact of model mismatch arising from data-driven modeling on control performance [27]. In [23, 28], offset-free Koopman Lyapunov-based MPC methods were proposed, and the stability of the resulting control designs was proven in the presence of plant-model mismatch.

The identification of a Koopman model involves the use of lifting functions to map the original nonlinear state-space into a higher-dimensional linear state-space. The selection of lifting functions can have a substantial impact on both the dimensionality and the accuracy of the resulting Koopman model. Many existing Koopman-based approaches [15, 22], including the representative extended dynamic mode decomposition [14, 19, 22], require a manual selection of the lifting functions based on experience/trial-and-error. However, the manual selection of suitable lifting functions for Koopman models can be very challenging. Additionally, even when appropriate lifting functions can be chosen, the resulting Koopman model will inevitably have a significantly higher dimensionality as compared to the original nonlinear process. While the nonlinear dynamics can be approximated by a linear state-space representation, it will be favorable to maintain the dimensionality of the Koopman model at a manageable level, from an analysis and control perspective. To ensure good prediction performance of the Koopman model and efficient computation of the associated Koopman-based control paradigm, it will be favorable to build an accurate and reasonably-dimensioned Koopman model for optimal control, which entails a systematic approach for selecting appropriate lifting functions, instead of relying on manual selection based on trial-and-error.

In the existing literature, to automate the selection of lifting functions for Koopman modeling, machine learning-based algorithms have been proposed [29–33]. The training of the involved neural networks typically requires large amounts of data. The concept of sparse identification of nonlinear dynamics (SINDy) and Kalman-based recursive algorithms have the potential to be leveraged to automatically select appropriate lifting functions for Koopman modeling. Specifically, SINDy provides a data-based sparse modeling framework, which finds the most active terms for a nonlinear model by solving sparse-promoting optimization [34–36]. This way, SINDy-based solutions can enhance the model interpretability while avoiding overfitting. In [37], instead of directly solving sparse-promoting optimization problems, a Kalman-based generalized SINDy (called Kalman-GSINDy) method was proposed to recursively identify the most relevant model terms from a library for con-

structuring sparse linear-in-parameter soft sensing models. The method in [37] provides a promising alternative pathway to recursively update the most appropriate lifting functions within the Koopman operator framework, instead of determining lifting functions manually based on trial-and-error or prior experience. In addition to automating the selection of Koopman lifting functions, we also aim to maintain the order of the resulting Koopman model via performing model reduction. In [29], deep learning-enabled Koopman modeling using an auto-encoder network was proposed for building reduced-order Koopman models for autonomous systems. Wiener-type Koopman model using deep auto-encoder has been proposed in [30], where control inputs were explicitly taken into account. These deep learning-based methods may require a large amount of data for training the neural networks, in order to achieve good model accuracy. Proper orthogonal decomposition (POD) has been widely used for extracting low-dimensional features of high-dimensional systems, which enables a reduction in the dimensionality of the system model being investigated [38–45]. We propose to integrate POD with the Koopman operator to create a reduced-order Koopman modeling framework, which provides linear approximation of nonlinear process dynamics while avoiding a significant increase in dimensionality.

In this work, we propose a data-driven reduced-order Koopman predictive control approach for general nonlinear systems. A Kalman-GSINDy approach is leveraged to select appropriate lifting functions from a comprehensive library. POD is exploited to propose a scalable data-driven Koopman identification approach, which can be used to obtain reduced-order Koopman linear models to approximate the dynamics of the underlying nonlinear process. A linear robust predictive control scheme is proposed based on the reduced-order Koopman model. The effectiveness of the proposed framework is demonstrated based on the application to a reactor-separator process. The superiority of the approach is illustrated in comparison to baselines. Some preliminary results of this work were submitted as a conference paper [46]. The current paper presents more detailed explanations and discussions of the proposed framework. In addition to simulation results considering the scenario with one single set-point presented in [46], the current paper also presents the simulation results considering the scenario with piece-wise constant set-points. Additionally, in the current paper, we include a detailed description of the benchmark process example and present comprehensive comparative results to illustrate the superiority of the proposed method.

## 2 Preliminaries

### 2.1 Koopman identification for controlled systems

Consider a controlled discrete-time nonlinear system of which the dynamics are described by the following nonlinear state-space form:

$$x_{k+1} = f(x_k, u_k) \quad (1)$$

where  $x_k \in \mathbb{X} \subset \mathbb{R}^n$  is the state vector at sampling instant  $k$ ,  $k = 1, \dots, K$ ;  $u_k \in \mathbb{U} \subset \mathbb{R}^m$  denotes the control input vector at sampling instant  $k$ ;  $\mathbb{X}$  and  $\mathbb{U}$  are two compact sets.

Based on the Koopman theory for controlled systems, the state is extended to  $\chi_k = [x_k^T, u_k^T]^T$ . There exists an infinite-dimensional nonlinear lifting mapping  $\Psi_\chi$ , such that the dynamics of the states in the lifted function space are governed by a Koopman operator denoted by  $\mathcal{K}$  as follows [14, 15, 48]:

$$\Psi_\chi(\chi_{k+1}) = \mathcal{K}\Psi_\chi(\chi_k) \quad (2)$$

where  $\Psi_\chi(\chi_k) := [\Psi(x_k)^T, u_k^T]^T$  with  $\Psi$  denotes a nonlinear mapping that operates on original state  $x$ . Instead of attempting to find the precise Koopman operator that can be of infinite dimension, a finite-dimensional nonlinear mapping  $\Psi : \mathbb{R}^n \rightarrow \mathbb{R}^N$  on state  $x$  can be considered, and the finite-dimensional Koopman operator  $\mathcal{K}$  can be identified on the finite-dimensional space accordingly. Additionally, finite-dimensional Koopman operator  $\mathcal{K}$  can be represented by a block matrix in the following form:

$$\mathcal{K} == \begin{bmatrix} A & B \\ * & * \end{bmatrix}. \quad (3)$$

We aim to forecast the dynamical behavior of  $\Psi$  using the Koopman operator instead of the entire vector  $\Psi_\chi$ . Therefore, it is sufficient to identify matrices  $A$  and  $B$ , which will enable the establishment of the following Koopman based linear model [14, 18, 47]:

$$\Psi(x_{k+1}) = A\Psi(x_k) + Bu_k. \quad (4)$$

### 2.2 Proper orthogonal decomposition

Proper orthogonal decomposition (POD) is a numerical method for obtaining a lower-dimensional approximated representation of a higher-dimensional system/process through data analysis [38].

Based on POD analysis, the original data samples can be expressed in an approximation form by choosing truncated basis vectors from all the basis vectors of the actual samples [39].

First, a coordinate transformation is conducted on the original state based on a projection matrix  $\Phi \in \mathbb{R}^{n \times n}$  that consists of a set of orthonormal basis vectors, that is,  $\Phi := [\phi_1, \phi_2, \dots, \phi_n]^T$  where  $\phi_i$ ,  $i = 1, \dots, n$  is the eigenvector of the covariance matrix based on the data samples. The eigenvalues of the covariance matrix are sorted in a descending order, such that  $\phi_i$  is the eigenvector corresponding to the  $i$ th largest eigenvalue.

Next, to reduce the order from  $n$  to  $r$ , the first  $r$  rows of  $\Phi$  (i.e., the eigenvectors that correspond to the  $r$  largest eigenvalues) are selected to form the reduced-order projection matrix  $\Phi_r \in \mathbb{R}^{r \times n}$ , i.e.,  $\Phi_r = [\phi_1, \phi_2, \dots, \phi_r]^T$ . Based on  $\Phi_r$ , a reduced-order coordinate transformation can be conducted to obtain a reduced-order approximation of the original state as follows:

$$q = \Phi_r v \quad (5)$$

where  $v \in \mathbb{R}^n$  denotes the original state vector; and  $q \in \mathbb{R}^r$  denotes the reduced-order state in the transformed coordinate.

This way, given a prescribed reduced order  $r$ ,  $r < n$ , POD establishes the optimal reduced-order projection matrix  $\Phi_r$  such that the distance between the original state vector  $v$  and its approximation  $\hat{v}$  is minimized as follows:

$$\min_{\Phi_r} \mathbb{E} \left\{ \|v - \hat{v}\|^2 \right\} \quad (6)$$

where  $\hat{v}$  is an approximation of  $v$  obtained through:

$$\hat{v} = \Phi_r^+ q = \Phi_r^T q. \quad (7)$$

Additionally,  $+$  denotes the matrix pseudo-inverse.

### 2.3 Problem formulation

The objective of this work is twofold: (a) to construct a reduced-order Koopman linear model to describe the dynamics of the nonlinear process in (1); (b) to develop a data-driven reduced-order Koopman predictive control scheme for set-point tracking in an efficient manner.

The reduced-order Koopman identification problem can be formulated as the following opti-

mization problem:

$$\min_{A_r, B_r, C, \Phi_r} \sum_{k=1}^{K-1} \|x_{k+1} - \hat{x}_{k+1}\|_2^2 \quad (8a)$$

$$\text{s.t. } \hat{q}_{k+1} = A_r \hat{q}_k + B_r u_k \quad (8b)$$

$$\hat{x}_k = C \hat{\Psi}(x_k) = C \Phi_r^T \hat{q}_k \quad (8c)$$

where  $\hat{q}_k \in \mathbb{R}^r$  denotes the state vector of the reduced-order Koopman model;  $\hat{\Psi}(x_k) \in \mathbb{R}^N$  denotes an approximation of the high-dimensional lifted state vector  $\Psi(x_k)$ ;  $\hat{x}_k \in \mathbb{R}^n$  denotes the predicted state given by the reduced-order Koopman model. The parameters to be identified include system matrices  $A_r \in \mathbb{R}^{r \times r}$  and  $B_r \in \mathbb{R}^{r \times m}$ , state reconstruction matrix  $C \in \mathbb{R}^{n \times N}$ , and reduce-order projection matrix  $\Phi_r \in \mathbb{R}^{r \times N}$ .

Based on a reduced-order linear Koopman model in the form of (8), linear model predictive control will be developed and implemented for the underlying nonlinear process in (1).

### 3 POD-based Koopman modeling using Kalman-GSINDy

This section presents the proposed reduced-order Koopman modeling method which integrates the Kalman-generalized sparse identification of nonlinear dynamics (Kalman-GSINDy) algorithm and proper orthogonal decomposition (POD).

#### 3.1 Architecture of the proposed mechanism

A graphical illustration of the proposed reduced-order Koopman modeling method is presented in Figure 1. Kalman-GINDy is leveraged to select appropriate lifting functions that map the original low-dimensional nonlinear state-space of system (1) to a higher-dimensional linear state-space. The left block in Figure 1 illustrates the idea of selecting lifting functions based on Kalman-GSINDy.  $\mathbf{L}$  is a function library containing all the candidate lifting functions.  $\Omega$  is a matrix of coefficients for all the candidate lifting functions with respect to the state variables of the original nonlinear process. Specifically, the  $i$ th column of  $\Omega$ , which is denoted by  $\xi_i$ , contains the coefficients for all the candidate lifting functions with respect to the  $i$ th variable of the state vector  $x$ . Kalman filter is used to recursively estimate  $\Omega$ . The estimate obtained in the final iteration step, denoted by  $\hat{\Omega}_K$ , will be used for selecting lifting functions for Koopman modeling.

The right block in Figure 1 illustrates the procedure of reduced-order Koopman modeling based

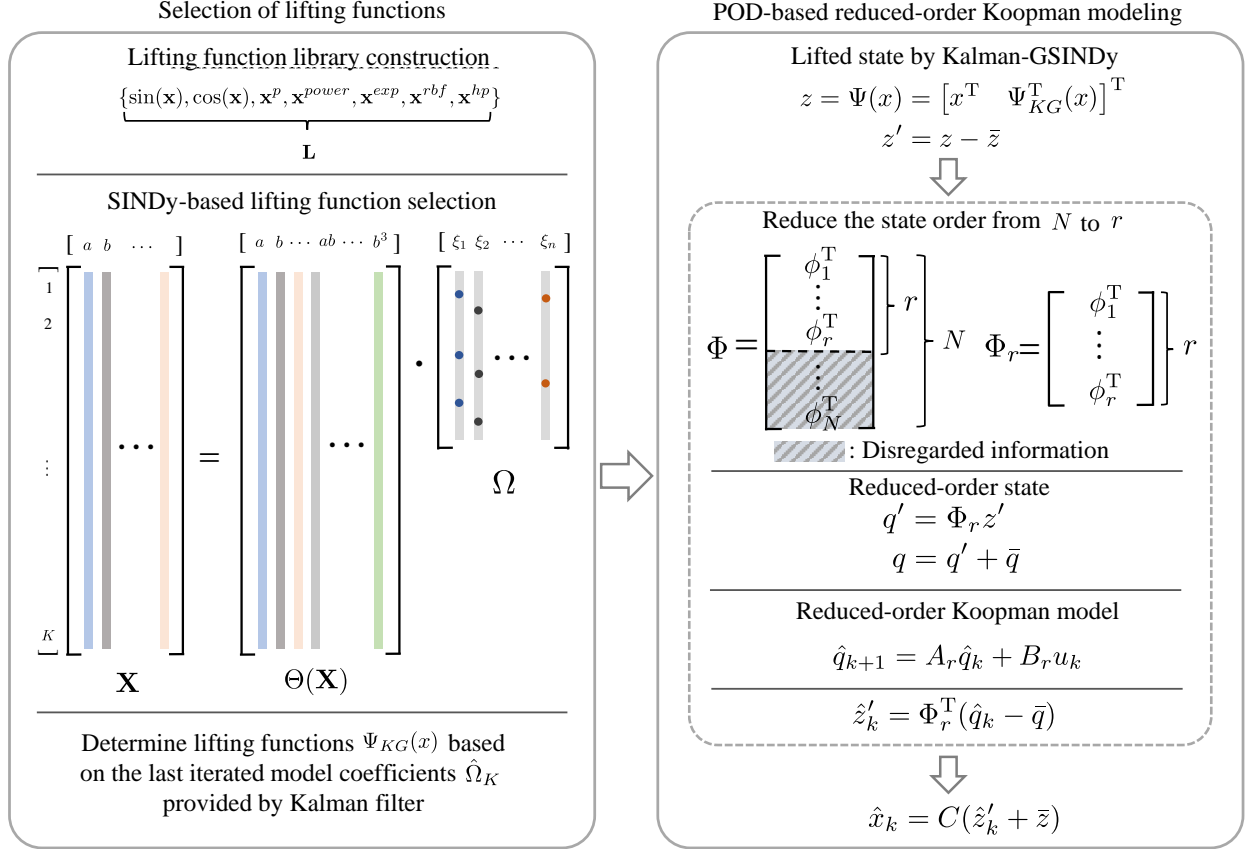


Figure 1: A graphical illustration of the proposed reduced-order Koopman model for control.

on POD. The higher-dimensional state vector  $z$  lifted by the selected lifting functions  $\Psi_{KG}$  is projected to a reduced-order state vector  $q$  through a projection matrix  $\Phi_r$  that is established by conducting POD analysis. Reduced-order Koopman operators  $A_r$  and  $B_r$  are identified to govern the evolution of  $q$  in the reduced-order linear state-space. The prediction of  $q$  (denoted by  $\hat{q}$ ) generated by the reduced-order Koopman model can be used to a predicted state of the original nonlinear process (denoted by  $\hat{x}$ ).

### 3.2 Kalman-GSINDy

In this subsection, Kalman-GSINDy is exploited to select appropriate lifting functions from an existing rich library as the basis of reduced-order Koopman identification.

In the first step, partially inspired by the existing literature relevant to Koopman modeling and the SINDy algorithm, a lifting function library  $\mathbf{L}$  that contains  $N_L$  candidate lifting functions is constructed [37]. With slight abuse of notation, we use row vector  $\mathbf{x} \in \mathbb{R}^{1 \times n}$  to denote the transpose



of  $x$ , i.e.,  $\mathbf{x} = x^T$ . A representative lifting function library  $\mathbf{L}$  can be created as follows:

$$\mathbf{L} = \{\sin(\mathbf{x}), \cos(\mathbf{x}), \mathbf{x}^p, \mathbf{x}^{power}, \mathbf{x}^{exp}, \mathbf{x}^{rbf}, \mathbf{x}^{hp}\} \quad (9)$$

where  $\mathbf{x}^p$  denotes all the terms of possible multiplications of the variables involved in vector  $\mathbf{x}$ , for example, if  $\mathbf{x} = [a, b, c]$ , then  $\mathbf{x}^p$  includes  $ab, ac, bc, abc$ ;  $\mathbf{x}^{power}$  denotes selected power functions;  $\mathbf{x}^{exp}$  denotes selected exponential functions;  $\mathbf{x}^{rbf}$  and  $\mathbf{x}^{hp}$  denote radial basis functions and Hermite polynomials, respectively [48, 49]. Note that with slight abuse of notation, each function in (9) conducts element-by-element operations for all the variables involved in  $\mathbf{x}$ , for example, for state vector  $\mathbf{x} = [a, b, c]$ ,  $\sin(\mathbf{x})$  returns  $[\sin(a), \sin(b), \sin(c)]$ .

The next step is to build the dataset matrix  $\mathbf{X}$  and lifted dataset matrix  $\Theta(\mathbf{X})$ .  $\mathbf{X} \in \mathbb{R}^{K \times n}$  denotes the matrix of all date samples that  $\mathbf{X} = [x_1, \dots, x_K]^T$ .  $\Theta(\mathbf{X}) \in \mathbb{R}^{K \times N_L}$  denotes the matrix of the lifted data values. The  $k$ th row of  $\Theta(\mathbf{X})$  is constituted by the values of the candidate lifting functions in  $\mathbf{L}$  calculated based on state measurement  $\mathbf{x}_k = x_k^T$ ,  $k = 1, \dots, K$ , at time instant  $k$  denoted as  $\Theta(\mathbf{x}_k)$ .

The unknown coefficients involved in  $\Omega$  are estimated recursively by leveraging the Kalman-GSINDy algorithm [37]. Specifically, as a new sample  $\mathbf{x}_k$  is provided, an updated estimate  $\hat{\Omega}_k$  is obtained through a Kalman-like two-step calculation:

*Prediction step :*

$$\hat{\Omega}_k^- = F_k \hat{\Omega}_{k-1} \quad (10a)$$

$$P_k^- = F_{k-1} P_{k-1} F_{k-1}^T + Q^* \quad (10b)$$

where  $\hat{\Omega}_{k-1}$  and  $\hat{\Omega}_k^-$  are the posterior and prior estimates of the coefficients for the candidate lifting functions;  $P_{k-1}$  and  $P_k^-$  denote the posterior and prior estimation error covariance matrices, respectively;  $F_k = I$  for  $k = 1, \dots, K$ ;  $Q^*$  is the covariance matrix of the process noise.

*Correction step :*

$$K_k = P_k^- \Theta(\mathbf{x}_k)^T \left( \Theta(\mathbf{x}_k) P_k^- \Theta(\mathbf{x}_k)^T + R^* \right)^{-1} \quad (11a)$$

$$\hat{\mathbf{x}}_k = \Theta(\mathbf{x}_k) \hat{\Omega}_k^- \quad (11b)$$

$$\hat{\Omega}_k = \hat{\Omega}_k^- + K_k (\mathbf{x}_k - \hat{\mathbf{x}}_k) \quad (11c)$$

$$P_k = (I - K_k \Theta(\mathbf{x}_k)) P_k^- \quad (11d)$$

where  $K_k$  is the Kalman gain;  $\hat{\mathbf{x}}_k$  represents the estimate of the original state  $\mathbf{x}_k$ ;  $\Theta(\mathbf{x}_k)$  is the lifted state value;  $R^*$  is the covariance matrix of the measurement noise.

The estimate of the coefficients obtained in the  $K$ th iteration step (where  $K$  is the total number of samples), referred to as  $\hat{\Omega}_K$ , is treated as the final estimate of  $\Omega$ , and is used to select appropriate lifting functions from library  $\mathbf{L}$  to create  $\Psi(x)$ . To ensure the estimates of unknown coefficients  $\Omega$  will converge and the most appropriate lifting functions will be selected from the library, sufficient data samples of the considered nonlinear process are required, that is,  $K$  needs to be sufficiently large.

As shown in Figure 1,  $\Psi(x)$  consists of two components given as follows:

$$\Psi(x) = \begin{bmatrix} x^T & \Psi_{KG}^T(x) \end{bmatrix}^T \quad (12)$$

where  $x$  is the original process state vector and  $\Psi_{KG}(x)$  is the vector of nonlinear lifting functions selected from the library based on  $\hat{\Omega}_K$ . To construct  $\Psi_{KG}(x)$ , a user-specified positive scalar  $\lambda$  is needed. The values of the elements in each row of  $\hat{\Omega}_K$  are compared with  $\lambda$ . If any of the elements in the  $i$ th row is greater than  $\lambda$ , then the  $i$ th candidate lifting function ( $i = 1, \dots, N_L$ ) will be selected and incorporated into  $\Psi_{KG}(x)$ . Additionally,  $z = \Psi(x)$  is determined as the state vector in the lifted state-space.

**Remark 1** *The library needs to be constructed in a way such that it contains a diverse range of candidate lifting functions. This ensures the resulting Koopman model, which is established based on the lifting functions selected from the library, can provide good prediction performance. The candidate lifting functions in (9) represent some of the commonly used functions. We adopt some of the monomials and trigonometric functions from the SINDy libraries considered in [34, 36, 37] to enrich our lifting function library. Exponential functions used in [22] for Koopman modeling were also adopted. To enrich the library with more potential candidate lifting functions, some other functions, such as radial basis functions [48] and Hermite polynomials [49] have been added to the lifting function library. The candidate lifting functions included in a library may be adjusted or enriched based on physical knowledge of the specific process being considered, experience of users, and/or trial-and-error analysis. It is noted that since only the most appropriate lifting functions will be selected from the candidate lifting functions in the library, further enriching the library with less relevant thus redundant candidate lifting functions will not likely affect the dimensionality of the resulting Koopman model significantly.*

### 3.3 POD-based reduced-order Koopman identification

In this subsection, POD is employed to reduce the dimensionality of the lifted linear state-space, and Koopman operator is identified in the reduced-order state-space to characterize the dynamics of the underlying nonlinear process.

After mean removal, zero-mean samples  $z' = z - \bar{z}$  (where  $\bar{z}$  represents the mean values of the lifted state  $z$ ), can be obtained. Considering (5), the zero-mean reduced-order state  $q' \in \mathbb{R}^r$  is given in the following form:

$$q' = \Phi_r z' \quad (13)$$

where  $\Phi_r \in \mathbb{R}^{r \times N}$  is the reduced-order projection matrix that can be determined following POD analysis in Section 2.2. The order  $r$  of the reduced-order Koopman model is a user-specified parameter, and it needs to be determined carefully based on trial-and-error to balance the trade-off between the model accuracy and the model dimensionality.

Additionally, the mean value of reduced-order state  $\bar{q}$  is computed as  $\bar{q} = \Phi_r \bar{z}$ . Based on (4), we consider the dynamic of the reduced-order state  $q \in \mathbb{R}^r$  where  $q = q' + \bar{q}$  is governed by reduced-order Koopman operator given as:

$$q_{k+1} = A_r q_k + B_r u_k. \quad (14)$$

To construct reduced-order Koopman operator  $A_r$  and  $B_r$ , the following batch least-squares problem is formulated:

$$\min_{A_r, B_r} \sum_{k=1}^{K-1} \|q_{k+1} - A_r q_k - B_r u_k\|_2^2. \quad (15)$$

Based on the technique adopted in [15], the analytical solution to (15) can be obtained:

$$[A_r, B_r] = \mathbf{q}_{k+1} \begin{bmatrix} \mathbf{q}_k \\ \mathbf{u}_k \end{bmatrix}^T \left( \begin{bmatrix} \mathbf{q}_k \\ \mathbf{u}_k \end{bmatrix} \begin{bmatrix} \mathbf{q}_k \\ \mathbf{u}_k \end{bmatrix}^T \right)^+ \quad (16)$$

where  $\mathbf{q}_k \in \mathbb{R}^{r \times K-1}$ ,  $\mathbf{q}_{k+1} \in \mathbb{R}^{r \times K-1}$ , and  $\mathbf{u}_k \in \mathbb{R}^{m \times K-1}$  are snapshot matrices in the forms of  $\mathbf{q}_k = [q_1, \dots, q_{K-1}]$ ,  $\mathbf{q}_{k+1} = [q_2, \dots, q_K]$ , and  $\mathbf{u}_k = [u_1, \dots, u_{K-1}]$ .

Based on (7), the relation between the zero-mean reduce-order state  $q'$  and the approximated

lifted state vector  $\hat{z}$  is described as follows:

$$\hat{z} = \Phi_r^T q' + \bar{z} = \Phi_r^T (q - \bar{q}) + \bar{z}. \quad (17)$$

Consequently, a reduced-order Koopman model that describes the dynamics of the nonlinear process (1) can be formulated:

$$\hat{q}_{k+1} = A_r \hat{q}_k + B_r u_k \quad (18a)$$

$$\hat{x}_k = C (\Phi_r^T (\hat{q}_k - \bar{q}) + \bar{z}) \quad (18b)$$

where  $\hat{q}_k$  denotes the predicted reduced-order state of the reduced-order Koopman model;  $\hat{x}_k$  denotes the predicted original state of the nonlinear process. In (18b), the projection matrix  $C$  is in the form of  $C = [I_{n \times n}, 0_{n \times N-n}]$ . This is because the vector of the lifting functions is determined as (12), and the first  $n$  elements of  $z$  are identical to the original nonlinear process states  $x$ .

**Remark 2** *The proposed method is a purely data-driven approach. If any first-principles knowledge is available, it may be favorable to integrate such knowledge with data seamlessly by proposing hybrid modeling approaches [50–53]. How physical knowledge can be incorporated into the Koopman modeling framework to form physics-enabled Koopman models will be considered in our future work.*

## 4 Robust MPC with reduced-order Koopman operators

In this section, we propose a robust model predictive control (MPC) scheme based on the reduced-order Koopman in (18) for nonlinear process (1). A block diagram of the proposed reduced-order Koopman robust MPC is presented in Figure 2.

First, an MPC design is formulated based on the identified reduced-order Koopman model in the nominal form of (18). The objective function  $J$  is formulated as follows:

$$J = \sum_{j=k}^{k+N_c-1} \ell (\hat{q}_{j|k} - q_s, \hat{u}_{j|k} - u_s) \quad (19)$$

where

$$\ell (\hat{q}_{j|k} - q_s, \hat{u}_{j|k} - u_s) = \|\hat{q}_{j|k} - q_s\|_Q^2 + \|\hat{u}_{j|k} - u_s\|_R^2 \quad (20)$$

In (20),  $Q \in \mathbb{R}^{r \times r}$  and  $R \in \mathbb{R}^{m \times m}$  are positive-definite weighting matrices;  $N_c$  is the control horizon;

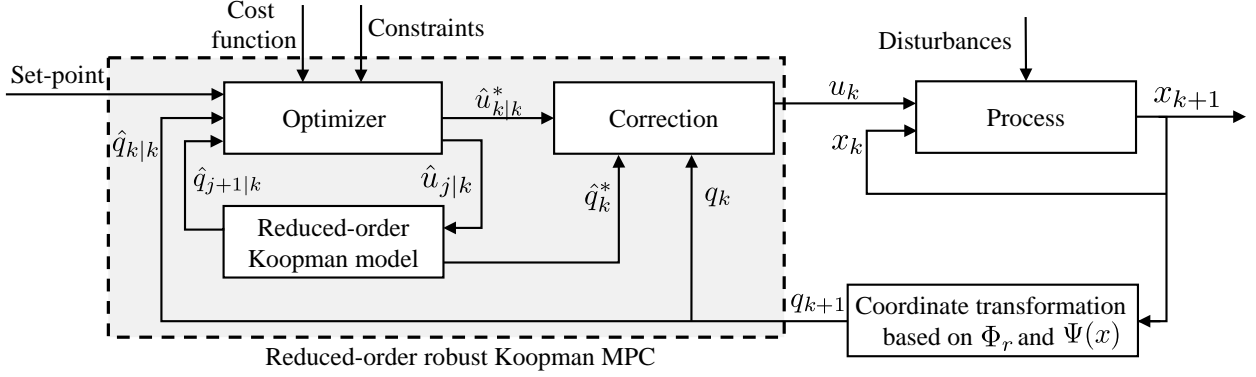


Figure 2: A block diagram of the reduced-order robust Koopman MPC.

$q_s$  represents the reduced-order state computed based on set-point state  $x_s$  that  $q_s = \Phi_r \Psi(x_s)$ ;  $u_s$  is the steady-state reference input corresponding to set-point  $x_s$ ;  $\hat{q}_{j|k}$  is a prediction of the reduced-order state for time instant  $j$  obtained at time instant  $k$ ;  $\hat{u}_{j|k}$  is the control input for sampling instant  $j$  calculated at time instant  $k$ ;  $\|x\|_Q^2$  is weighted Euclidean norm of vector  $x$ , computed as  $\|x\|_Q^2 := x^T Q x$ . Based on the objective function in (19), a reduced-order MPC design is formulated as follows:

$$\min_{\hat{u}_{k|k}, \dots, \hat{u}_{k+N_c-1|k}} J \quad (21a)$$

$$\text{s.t. } \hat{q}_{j+1|k} = A_r \hat{q}_{j|k} + B_r \hat{u}_{j|k}, \quad (21b)$$

$$\hat{q}_{k|k} = \Phi_r \Psi(x_k), \quad (21c)$$

$$C(\Phi_r^T(\hat{q}_{j|k} - \bar{q}) + \bar{z}) \in \mathbb{X}, \quad (21d)$$

$$\hat{u}_{j|k} \in \mathbb{U}, \quad j = k, \dots, k + N_c - 1. \quad (21e)$$

In (21),  $\hat{u}_{k|k}, \dots, \hat{u}_{k+N_c-1|k}$  denotes the control input sequence;  $q_k$  is the reduced-order state obtained from the state measurement  $x_k$  at time  $k$ . The optimal solution to problem (21) at time instant  $k \in \mathbb{N}$  is represented by:

$$\hat{u}_{k|k}^*, \hat{u}_{k+1|k}^*, \dots, \hat{u}_{k+N_c-1|k}^*. \quad (22)$$

The first control action  $\hat{u}_{k|k}^*$  in the optimal control sequence in (22) is applied to the reduced-order Koopman model in (18a) to generate predicted state  $\hat{q}_{k+1}^*$ , which will be further used to compute the optimal control action that needs to be applied to the nonlinear process in (1). Then, to account

for the model mismatch between the reduced-order Koopman model and the actual dynamics of the nonlinear process (1), a stochastic version of the reduced-order Koopman linear model is presented as follows:

$$q_{k+1} = A_r q_k + B_r u_k + w_k \quad (23a)$$

$$x_k = C \left( \Phi_r^T (q_k - \bar{q}) + \bar{z} \right) + v_k \quad (23b)$$

where  $w_k$  and  $v_k$  account for time-varying model uncertainties. We assume that the model uncertainties  $w_k$  and  $v_k$  are bounded such that  $w_k \in \mathbb{W}$ ,  $v_k \in \mathbb{V}$ ,  $\forall k \in \mathbb{N}$  where  $\mathbb{W}$  and  $\mathbb{V}$  are compact sets. Note that this type of assumption on the boundedness of the system uncertainties was also made in relevant work on robust MPC, see, e.g., [20, 54].

The error between the actual and nominal reduced-order state, i.e., (23a) and (18a), is computed as:

$$e_{k,q} = q_k - \hat{q}_k^* \quad (24)$$

To account for the model uncertainties of the reduced-order Koopman model, following the robust MPC algorithm in [20], we introduce a state-feedback control and form the actual controller output  $u_k$  as:

$$u_k = \hat{u}_{k|k}^* + K_r e_{k,q} \quad (25)$$

where  $K_r \in \mathbb{R}^{m \times r}$  is the state-feedback gain matrix.

Based on (25), the error dynamics of  $e_{k,q}$  can be expressed as  $e_{k+1,q} = A_K e_{k,q} + w_k$ , where  $A_K := A_r + B_r K_r$ . If  $K_r$  is determined appropriately such that  $A_K$  is Schur stable, then the error dynamics are stable, and the tracking error asymptotically converges to zero.

## 5 Application to a reactor-separator process

In this section, we apply the proposed method to a benchmark chemical reaction process via simulations to illustrate the proposed framework.

### 5.1 Process description and process operation objective

The benchmark chemical process involves two continuous stirred reactors (CSTRs) and one flash tank separator; a schematic diagram of this process is presented in Figure 3. In this process, two

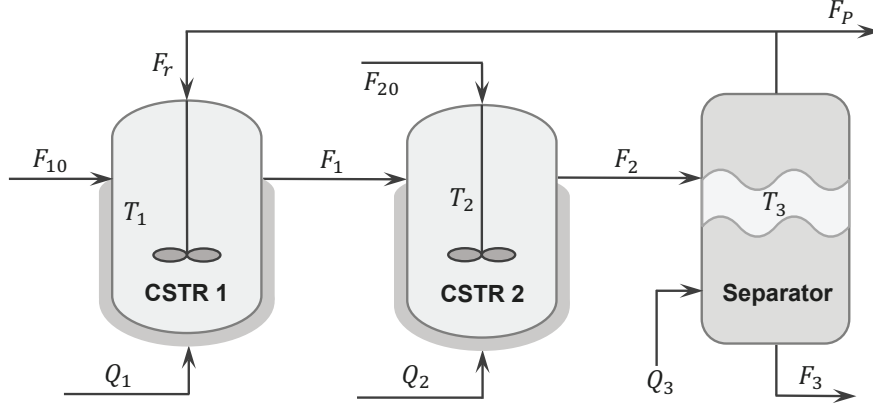


Figure 3: Reactor-separator process.

irreversible reactions take place simultaneously: the conversion of reactant **A** into desired product **B**, and the conversion of a portion of **B** into side product **C**. The three vessels of this process are interconnected with each other through mass and energy flows. Specifically, a fresh feed flow carrying pure reactant **A** is introduced into the first CSTR (CSTR 1) with volumetric flow rate  $F_{10}$  and temperature  $T_{10}$ . The output stream from CSTR 1 flows into the second CSTR (CSTR 2); another feed stream carrying pure **A** enters CSTR 2 at flow rate  $F_{20}$  and temperature  $T_{20}$ . The two chemical reactions  $\mathbf{A} \rightarrow \mathbf{B}$  and  $\mathbf{B} \rightarrow \mathbf{C}$  take place in the two CSTRs. The effluent from CSTR 2 is directed to the separator at flow rate  $F_2$  and temperature  $T_2$  [12, 55].

The separator provides a recycle stream that re-enters the first vessel at flow rate  $F_r$  and temperature  $T_3$ . Each of the three vessels is equipped with a heating jacket, which is used to add heat to or remove heat from the corresponding vessel at a variable heat input rate  $Q_i$ ,  $i = 1, 2, 3$ . The state variables of this nonlinear include the mass fractions of materials **A** and **B**, denoted by  $X_{\mathbf{A}i}$  and  $X_{\mathbf{B}i}$ , and the temperatures  $T_i$ ,  $i = 1, 2, 3$ , in the three vessels. Nine ordinary differential equations have been established based on the materials and energy balances to characterize the dynamical behaviors of the process states, which are shown as follows [12, 55, 56]:

$$\frac{dx_{\mathbf{A}1}}{dt} = \frac{F_{10}}{V_1}(x_{\mathbf{A}10} - x_{\mathbf{A}1}) + \frac{F_r}{V_1}(x_{\mathbf{A}r} - x_{\mathbf{A}1}) - k_1 e^{\frac{-E_1}{rT_1}} x_{\mathbf{A}1} \quad (26a)$$

$$\frac{dx_{\mathbf{B}1}}{dt} = \frac{F_{10}}{V_1}(x_{\mathbf{B}10} - x_{\mathbf{B}1}) + \frac{F_r}{V_1}(x_{\mathbf{B}r} - x_{\mathbf{B}1}) + k_1 e^{\frac{-E_1}{rT_1}} x_{\mathbf{A}1} - k_2 e^{\frac{-E_2}{rT_1}} x_{\mathbf{B}1} \quad (26b)$$

$$\frac{dT_1}{dt} = \frac{F_{10}}{V_1}(T_{10} - T_1) + \frac{F_r}{V_1}(T_3 - T_1) - \frac{\Delta H_1}{c_p} k_1 e^{\frac{-E_1}{rT_1}} x_{\mathbf{A}1} - \frac{\Delta H_2}{c_p} k_2 e^{\frac{-E_2}{rT_1}} x_{\mathbf{B}1} + \frac{Q_1}{\rho c_p V_1} \quad (26c)$$

$$\frac{dx_{\mathbf{A}2}}{dt} = \frac{F_1}{V_2}(x_{\mathbf{A}1} - x_{\mathbf{A}2}) + \frac{F_{20}}{V_2}(x_{\mathbf{A}20} - x_{\mathbf{A}2}) - k_1 e^{\frac{-E_1}{rT_2}} x_{\mathbf{A}2} \quad (26d)$$

$$\frac{dx_{\mathbf{B}2}}{dt} = \frac{F_1}{V_2}(x_{\mathbf{B}1} - x_{\mathbf{B}2}) + \frac{F_{20}}{V_2}(x_{\mathbf{B}20} - x_{\mathbf{B}2}) + k_1 e^{\frac{-E_1}{rT_2}} x_{\mathbf{A}2} - k_2 e^{\frac{-E_2}{rT_2}} x_{\mathbf{B}2} \quad (26e)$$

$$\frac{dT_2}{dt} = \frac{F_1}{V_2}(T_1 - T_2) + \frac{F_{20}}{V_2}(T_{20} - T_2) - \frac{\Delta H_1}{c_p} k_1 e^{\frac{-E_1}{rT_2}} x_{\mathbf{A}2} - \frac{\Delta H_2}{c_p} k_2 e^{\frac{-E_2}{rT_2}} x_{\mathbf{B}2} + \frac{Q_2}{\rho c_p V_2} \quad (26f)$$

$$\frac{dx_{\mathbf{A}3}}{dt} = \frac{F_2}{V_3}(x_{\mathbf{A}2} - x_{\mathbf{A}3}) - \frac{(F_r + F_p)}{V_3}(x_{\mathbf{A}r} - x_{\mathbf{A}3}) \quad (26g)$$

$$\frac{dx_{\mathbf{B}3}}{dt} = \frac{F_2}{V_3}(x_{\mathbf{B}2} - x_{\mathbf{B}3}) - \frac{(F_r + F_p)}{V_3}(x_{\mathbf{B}r} - x_{\mathbf{B}3}) \quad (26h)$$

$$\frac{dT_3}{dt} = \frac{F_2}{V_3}(T_2 - T_3) + \frac{Q_3}{\rho c_p V_3} + \frac{(F_r + F_p)}{\rho c_p V_3}(x_{\mathbf{A}r} \Delta H_{\text{vap}1} + x_{\mathbf{B}r} \Delta H_{\text{vap}2} + x_{\mathbf{C}r} \Delta H_{\text{vap}3}) \quad (26i)$$

In addition, the algebraic equations that describe the relationship between the composition of the overhead stream and the composition of the liquid holdup in the separator are given as follows:

$$\begin{aligned} x_{\mathbf{A}r} &= \frac{\alpha_{\mathbf{A}} x_{\mathbf{A}3}}{\alpha_{\mathbf{A}} x_{\mathbf{A}3} + \alpha_{\mathbf{B}} x_{\mathbf{B}3} + \alpha_{\mathbf{C}} x_{\mathbf{C}3}} \\ x_{\mathbf{B}r} &= \frac{\alpha_{\mathbf{B}} x_{\mathbf{B}3}}{\alpha_{\mathbf{A}} x_{\mathbf{A}3} + \alpha_{\mathbf{B}} x_{\mathbf{B}3} + \alpha_{\mathbf{C}} x_{\mathbf{C}3}} \\ x_{\mathbf{C}r} &= \frac{\alpha_{\mathbf{C}} x_{\mathbf{C}3}}{\alpha_{\mathbf{A}} x_{\mathbf{A}3} + \alpha_{\mathbf{B}} x_{\mathbf{B}3} + \alpha_{\mathbf{C}} x_{\mathbf{C}3}} \end{aligned} \quad (27)$$

The definitions for the process variables are given in Table 1. A detailed description of this chemical process and the values of the model parameters can be found in [12, 55].

The objective is: 1) to establish a Koopman linear model of a moderate dimensionality to describe the dynamics of the nonlinear chemical process; 2) to drive the process operation to desired set-points by regulating the heat inputs  $Q_i$ ,  $i = 1, 2, 3$ , applied to the three vessels.

## 5.2 Simulation setting

The liquid hold-up in each of the three vessels remains at a constant level during the process operation. We consider two open-loop stable steady-state levels as the set-points to illustrate the proposed framework. The two set-points  $x_{s1}$  and  $x_{s2}$  are shown in Table 2. Each of the set-points is corresponding to one steady-state level of heat inputs, which is presented in Table 3.

The state measurements are sampled asynchronously at time instant  $k$  with a sampling period of 0.025 hours. First, open-loop simulations are conducted to generate data for Koopman modeling. The heat inputs applied to the three vessels are generated randomly in a uniform distribution within the prescribed ranges and are varied after every 1.5 hours, which are shown in Figure 4.



Table 1: Process variables.

$x_{A1}, x_{A2}, x_{A3}$	Mass fractions of <b>A</b> in CSTR 1, CSTR 2, separator
$x_{B1}, x_{B2}, x_{B3}$	Mass fractions of <b>B</b> in CSTR 1, CSTR 2, separator
$x_{C3}, x_{C3}, x_{C3}$	Mass fractions of <b>C</b> in CSTR 1, CSTR 2, separator
$x_{Ar}, x_{Br}, x_{Cr}$	Mass fractions of <b>A</b> , <b>B</b> , <b>C</b> in the recycle stream
$x_{A10}, x_{B10}$	Mass fractions of <b>A</b> , <b>B</b> in the feed flows
$T_1, T_2, T_3$	Temperatures in CSTR 1, CSTR 2, separator
$T_{10}, T_{20}$	Feed stream temperatures to CSTR 1, CSTR 2, separator
$F_1, F_2$	Effluent flow rates from CSTR 1, CSTR 2
$F_{10}, F_{20}$	Steady-state feed stream flow rates to CSTR 1, CSTR 2
$F_r, F_p$	Flow rates of the recycle and purge streams
$V_1, V_2, V_3$	Volumes of CSTR 1, CSTR 2, separator
$E_1, E_2$	Activation energy for reactions <b>A</b> $\rightarrow$ <b>B</b> , <b>B</b> $\rightarrow$ <b>C</b>
$k_1, k_2$	Pre-exponential values for reactions <b>A</b> $\rightarrow$ <b>B</b> , <b>B</b> $\rightarrow$ <b>C</b>
$\Delta H_1, \Delta H_2$	Heats of reaction for reactions <b>A</b> $\rightarrow$ <b>B</b> , <b>B</b> $\rightarrow$ <b>C</b>
$\Delta H_{vap1}, \Delta H_{vap2}, \Delta H_{vap3}$	Evaporating enthalpies for <b>A</b> , <b>B</b> , <b>C</b>
$\alpha_A, \alpha_B, \alpha_C$	Relative volatilities of <b>A</b> , <b>B</b> , <b>C</b>
$Q_1, Q_2, Q_3$	Heat inputs into CSTR 1, CSTR 2, separator
$c_p, r, \rho$	Heat capacity, gas constant and solution density

Table 2: The initial state  $x_0$  and the two set-points  $x_{s1}, x_{s2}$ .

States	$x_{A1}$	$x_{B1}$	$T_1$ (K)	$x_{A2}$	$x_{B2}$	$T_2$ (K)	$x_{A3}$	$x_{B3}$	$T_3$ (K)
$x_0$	0.1155	0.6235	497.3	0.1367	0.6053	489.8	0.0396	0.5504	491.8
$x_{s1}$	0.1921	0.6753	476.8	0.2117	0.6561	468.5	0.0721	0.6896	471.5
$x_{s2}$	0.1336	0.6475	491.4	0.1547	0.6284	483.9	0.0469	0.5956	486.0

Table 3: Heat inputs  $u_{s1}, u_{s2}$  corresponding to the set-points  $x_{s1}, x_{s2}$ .

Heat inputs	$Q_1$ (kJ/h)	$Q_2$ (kJ/h)	$Q_3$ (kJ/h)
$u_{s1}$	$2.87 \times 10^6$	$1.00 \times 10^6$	$2.87 \times 10^6$
$u_{s2}$	$2.94 \times 10^6$	$1.14 \times 10^6$	$2.95 \times 10^6$

Table 4: The upper bounds and lower bounds of heat inputs  $u_{max}, u_{min}$ .

Bounds of heat inputs	$Q_1$ (kJ/h)	$Q_2$ (kJ/h)	$Q_3$ (kJ/h)
$u_{max}$	$2.976 \times 10^6$	$1.026 \times 10^6$	$2.976 \times 10^6$
$u_{min}$	$2.85 \times 10^6$	$0.98 \times 10^6$	$2.85 \times 10^6$

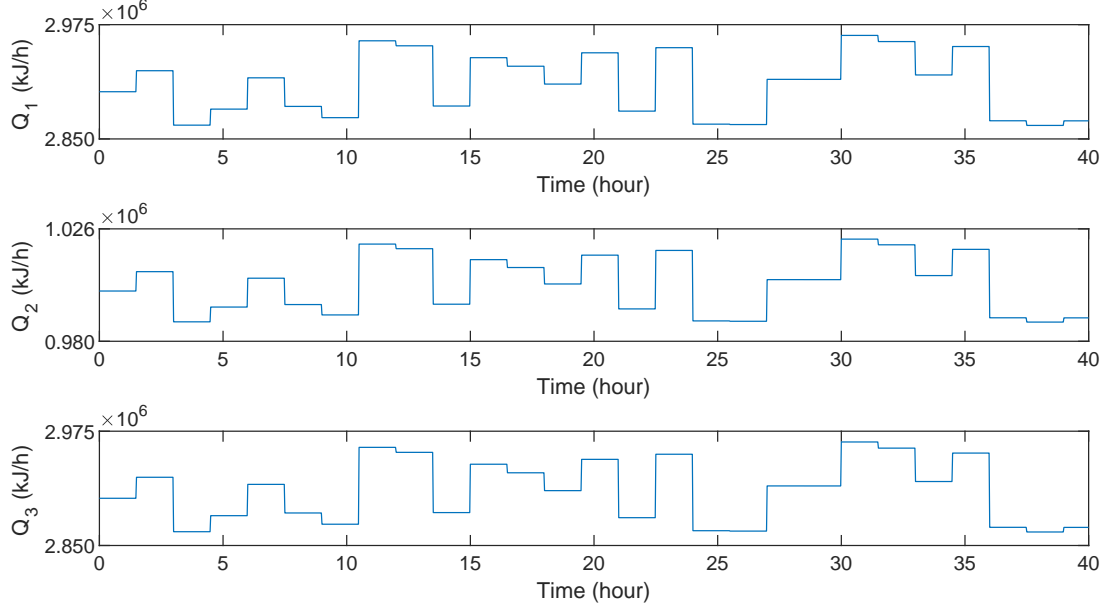


Figure 4: Trajectories of the heat inputs generated for modeling.

The upper bounds and lower bounds on the open-loop heat inputs are shown in Table 4. Bounded random disturbances are added to the process. The disturbances added to the dynamics of the concentrations are generated as normally distributed values with zero mean and a standard deviation of 1, and are then made bounded within the interval  $[-0.5, 0.5]$ . The disturbances added to the dynamics of the temperature are generated as normally distributed values with a zero mean and a standard deviation of 10, and are then made bounded within  $[-5, 5]$ .

The construction of the library  $\mathbf{L}$  is guided by (9). Specifically, the library comprises power functions and exponential functions including  $\mathbf{x}^{-0.5}$ ,  $\mathbf{x}^{0.5}$ ,  $\mathbf{x}^2$ ,  $\mathbf{x}^{2.5}$ ,  $\mathbf{x}^3$ ,  $\dots$ ,  $\mathbf{x}^5$ ,  $(1 + 0.25\mathbf{x}^2)^{-0.5}$ ,  $(1 + 0.25\mathbf{x}^2)^{0.5}$ ,  $e^{\mathbf{x}}$ ,  $e^{-0.2\mathbf{x}^2}$ , and  $\mathbf{x}^p$ ,  $\mathbf{x}^{rbf}$ , and  $\mathbf{x}^{hp}$  functions.

### 5.3 Reduced-order Koopman modeling

By implementing the Kalman-GSINDy algorithm, 16 lifting functions are selected from the library containing 610 lifting functions, which include the original state variables of the nonlinear process (1), and 7 lifting functions  $\Psi_{KG}(x) = [x_{(1)}x_{(3)}x_{(4)}, x_{(1)}x_{(3)}x_{(4)}x_{(6)}, x_{(3)}x_{(5)}x_{(6)}x_{(7)}, x_{(5)}x_{(7)}x_{(8)}x_{(9)}, x_{(1)}x_{(2)}x_{(4)}x_{(7)}x_{(8)}, x_{(2)}x_{(3)}x_{(6)}x_{(7)}x_{(9)}, \Pi_{i=1}^9 x_{(i)}]^T$ , where  $x_{(i)}$  denotes the  $i$ th variable of state vector  $x$ . Then, after applying the proposed reduced-order Koopman modeling approach, the order is reduced from 16 to 8 and a reduced-order Koopman linear model with 8 latent state variables is constructed.

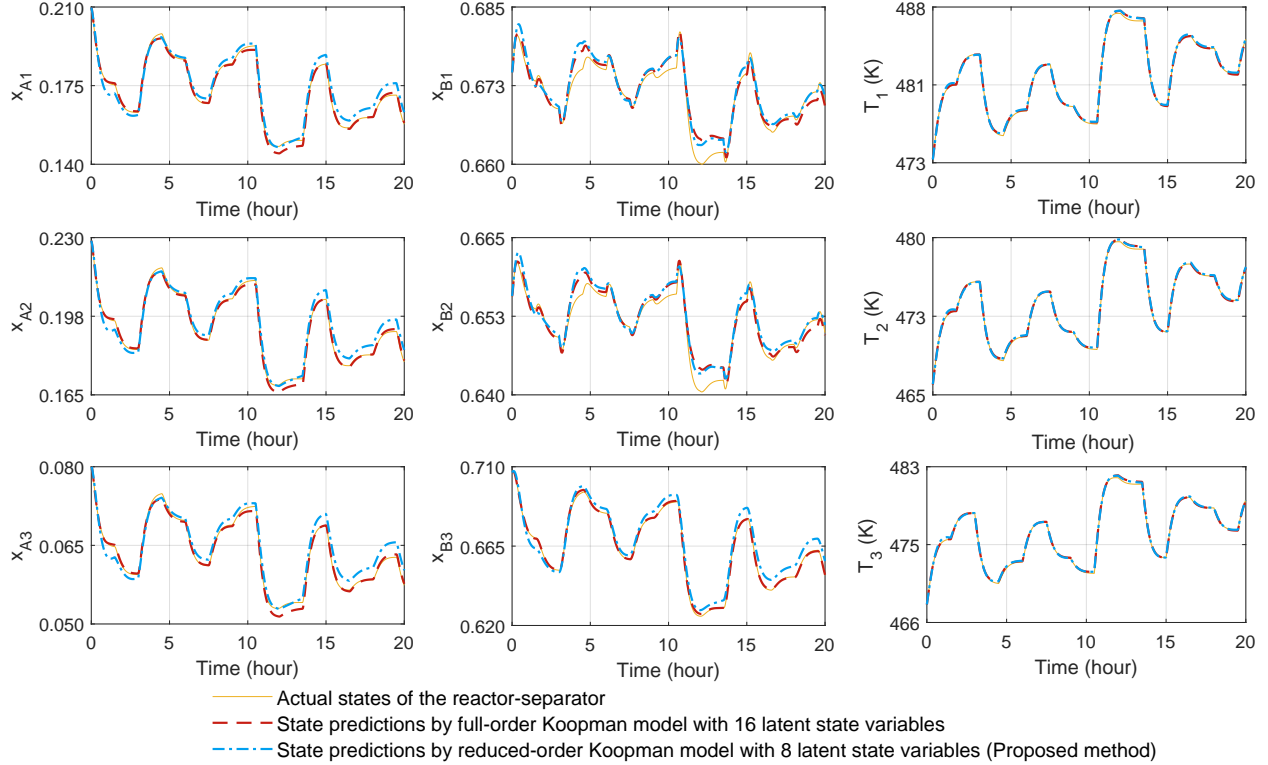
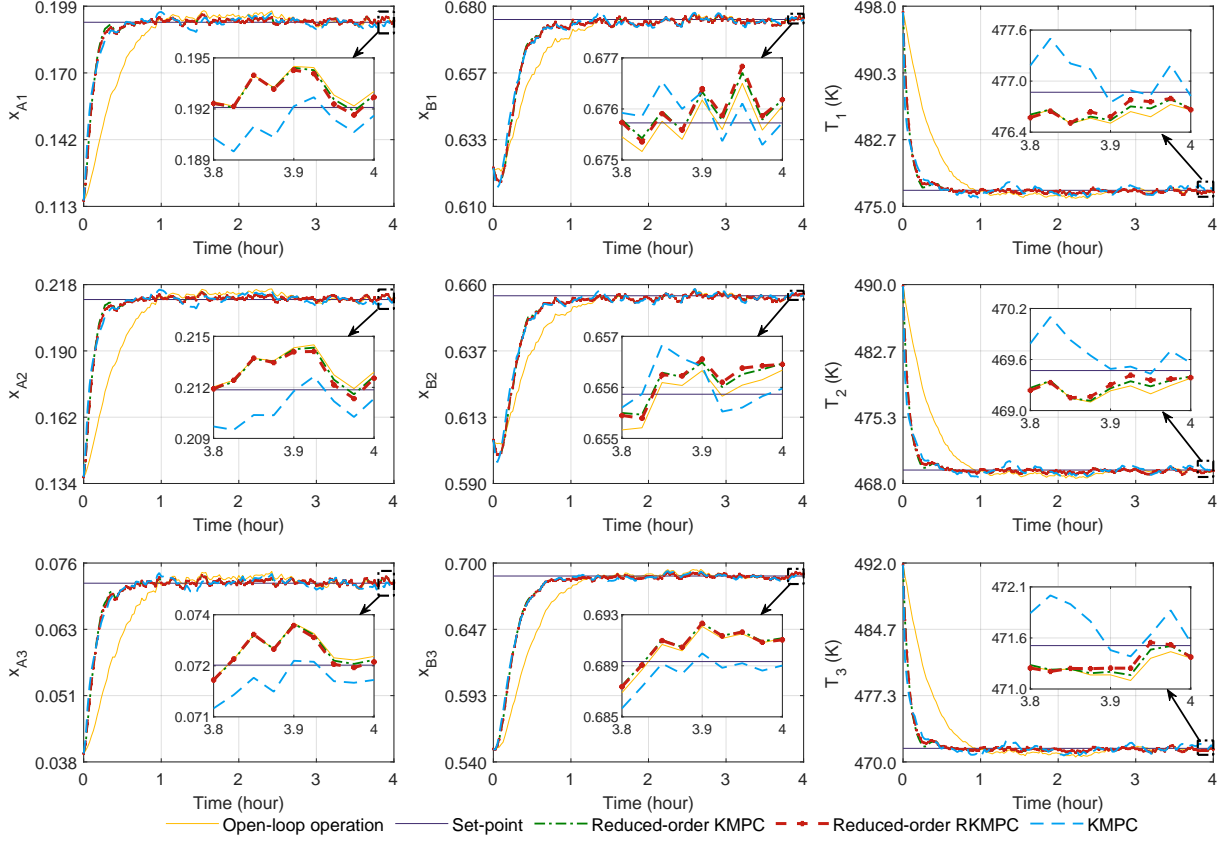


Figure 5: Prediction trajectories under the full-order Koopman and reduced-order Koopman model. The order of the full-order Koopman state is  $N = 16$ , and the order of the reduced-order Koopman state is  $r = 8$ .

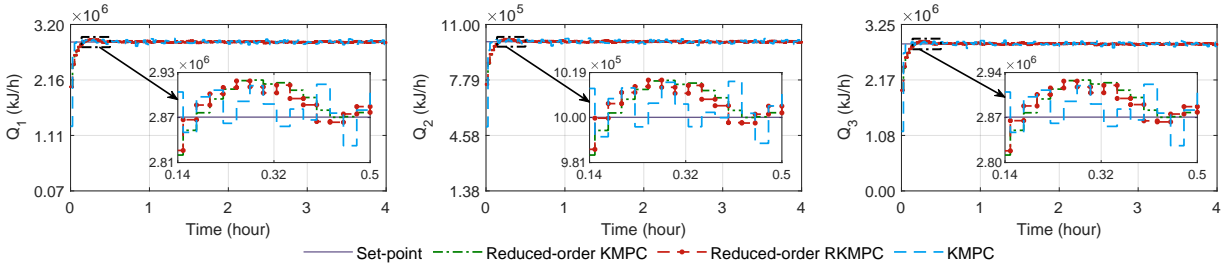
The open-loop predictions of the state variables of the reactor-separator process given by the proposed method, and the actual state trajectories are shown in Figure 5. The predictions (in blue dash-dotted lines) of the reduced-order Koopman model can track the trends of actual state trajectories. For comparison, Figure 5 also shows the state predictions of a full-order Koopman model with 16 latent state variables. This model is constructed based on the same lifting functions adopted in reduced-order Koopman modeling, yet it does not perform model order reduction. This full-order Koopman model provides slightly better prediction accuracy than the proposed method. However, the usage of a full-order Koopman model will lead to a significant increase in the computational complexity for the associated MPC, which will be discussed in Section 5.5.

## 5.4 Control performance

In this section, we evaluate and compare three control schemes: the proposed reduced-order robust Koopman MPC (reduced-order RKMP); reduced-order Koopman MPC (reduced-order KMPC); full-order Koopman MPC (full-order KMPC) without model reduction. The control objective is to



(a) State trajectories under the full-order KMPC, reduced-order KMPC, and reduced-order RKMPC.

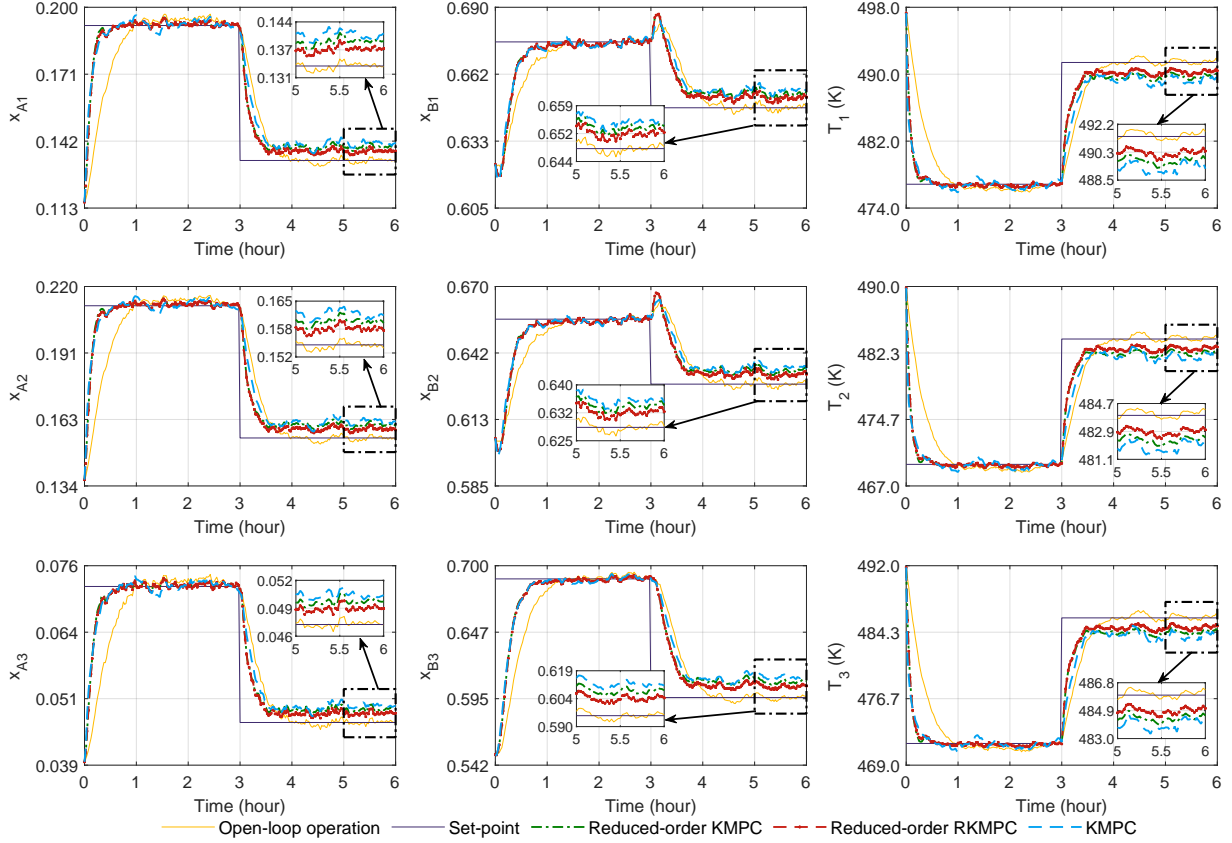


(b) Manipulated input trajectories under the full-order KMPC, reduced-order KMPC, and reduced-order RKMPC.

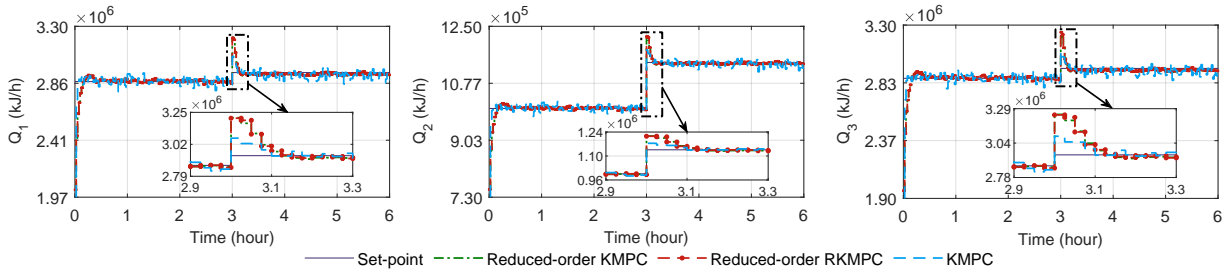
Figure 6: State and manipulated input trajectories with one single set-point.

track the set-points  $x_{s1}$  and  $x_{s2}$  given in Table 2, and maintain the process operation around the respective level. Two different case scenarios are considered to evaluate the control performance of different control schemes, that is, the case scenario with one single set-point  $x_{s1}$  to track, and the case scenario with a change in the set-point from  $x_{s1}$  to  $x_{s2}$  after three-hour process operation.

The control horizons for the three control designs are set as  $N_c = 15$ . For the full-order KMPC, the weighting matrices are  $Q_{full} = \text{diag}([12.34, 7.21, 8.44, 10.45, 11.23, 9.22, 10.23, 6.44, 8.54, 12.45, 9.32, 13.43, 12.43, 9.54, 11.32, 8.23]) \in \mathbb{R}^{16 \times 16}$  and  $R_{full} = \text{diag}([2.8, 3.3, 2.6]) \in \mathbb{R}^{3 \times 3}$ , where  $\text{diag}(\cdot)$



(a) State trajectories under the full-order KMPC, reduced-order KMPC, and reduced-order RKMPC.

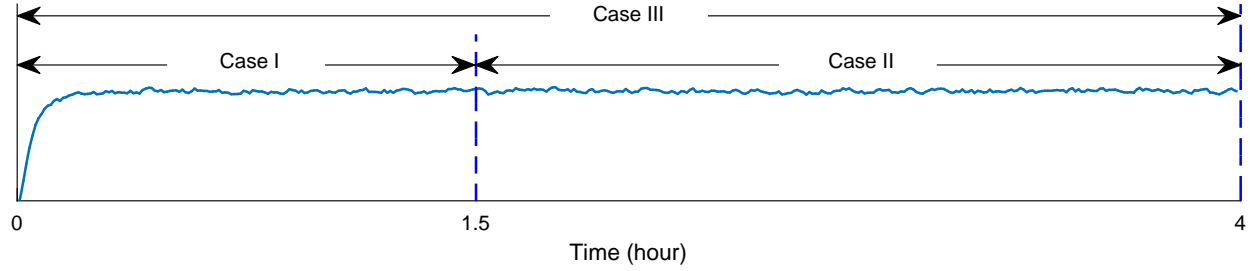


(b) Manipulated input trajectories under the full-order KMPC, reduced-order KMPC, and reduced-order RKMPC.

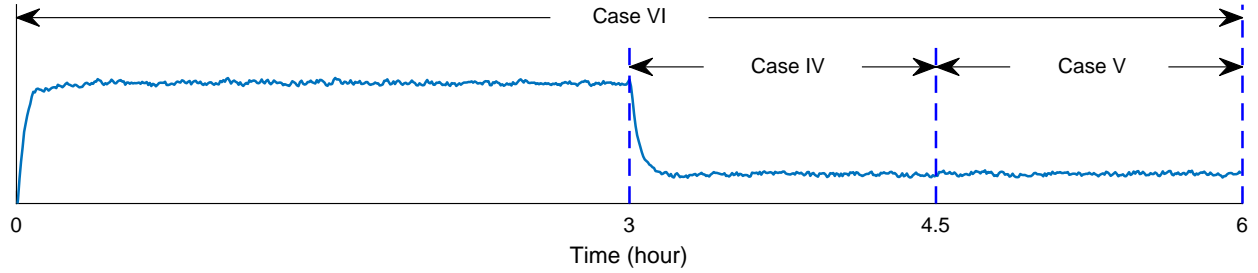
Figure 7: State and manipulated input trajectories with a change in set-point.

denotes a diagonal matrix. The weighting matrices of the reduced-order KMPC and RKMPC models are  $Q_{reduced} = \text{diag}([37.34, 38.21, 40.44, 49.45, 48.23, 37.22, 38.23, 31.44]) \in \mathbb{R}^{8 \times 8}$  and  $R_{reduced} = \text{diag}([2.8, 3.3, 2.6]) \in \mathbb{R}^{3 \times 3}$ .

First, we consider the case when only  $x_{s1}$  is considered as the reference to track. Figure 6(a) presents the closed-loop state trajectories generated by the three controllers, while Figure 6(b) presents the corresponding control input trajectories given by the three controllers. All the three control designs are able to steer the process states towards the desired set-point, and maintain the



(a) 3 RMSEs of different operating periods under the scenario with one single set-point.



(b) 3 RMSEs of different operating periods under the scenario with a change in the set-point.

Figure 8: A graphical illustration of the 6 RMSEs for different operating periods under the two case scenarios.

Table 5: Control performance comparison in terms of RMSEs under different cases and operating periods (each of the RMSE values that are highlighted in bold represents the best result among the three controllers under the same case).

	Case I	Case II	Case III	Case IV	Case V	Case VI
Full-order KMPC	<b>0.2520</b>	0.0189	<b>0.1550</b>	0.2436	0.1012	0.1786
Reduced-order KMPC	0.2631	0.0141	0.1615	0.2199	0.0801	0.1718
Reduced-order RKMPC	0.2639	<b>0.0135</b>	0.1620	<b>0.2134</b>	<b>0.0565</b>	<b>0.1676</b>

operation level close to the set-point.

Figure 7 presents the closed-loop state trajectories under the other case scenario with set-point change during process operation. Figure 7(a) presents the closed-loop state trajectories generated by the three controllers, and Figure 7(b) presents the trajectories of the control inputs by the three controllers. All the three controllers are capable of tracking the piecewise-constant set-points. The proposed reduced-order RKMPC outperforms the other two designs in the sense that it can bring the closed-loop states closer to the reference values.

To quantitatively assess and compare the control performance, six operating periods under the two case scenarios (with one single set-point, and with a change in the set-point, respectively) are

Table 6: Comparison of computation time.

Control method	Computation time (s/step)
Full-order KMPC	0.0734
Reduced-order KMPC	0.0405
Reduced-order RKMPC	0.0407

taken into account. We call them Cases I to VI, which are illustrated in Figure 8. Case I, II, and III are defined for a scenario with one single set-point: specifically, Case I considers the first 1.5-hour operation which includes the transient period; Case II considers a 2.5-hour steady-state operation; Case III covers the entire 4-hour operation period. Case IV, V, and VI are defined for another operating condition when there is a change in the set-point: Case IV covers a 1.5-hour period during which the process operation is steered towards the second set-point; Case V considers a 1.5-hour steady-state operation corresponding to the second set-point; Case VI considers the entire 6-hour operation. We compute the root mean squared errors (RMSE) for each of the controllers under the six cases to evaluate the tracking performance. The RMSE is defined as  $\text{RMSE} = \sqrt{\frac{1}{nK} \sum_{k=1}^K \|x_s - x_k\|_2^2}$ . Note that since the different magnitudes of the process states, the RMSEs are computed based on scaled system state values for a fair comparison.

The RMSE results for the three controllers under the six considered cases are presented in Table 5. The proposed reduced-order RKMPC outperforms the other two control methods in four cases out of the six cases. As compared to the full-order KMPC, the proposed reduced-order RKMPC exhibits comparable performance under the scenario with one single set-point and provides better set-point tracking performance under the scenario with a change in set-point. Additionally, the performance of the proposed reduced-order RKMPC is (slightly) better than reduced-order KMPC under Cases II and V.

## 5.5 Computation time comparison

Additionally, the Computation time for the three designs are compared. To ensure a fair comparison of the results, we compute the time costs of the transient-period (first 1.5 hours) with the constant set-point in the simulations. The computation time for one step of each control model is measured through multiple experiments. The simulations are conducted on a PC with an Intel® Core™ i7-12700 CPU of 12 cores.

Table 6 presents the average computation time needed for one-time execution of each of the three

control methods. Owing to the reduction in the dimensionality of the model orders as compared to the full-order Koopman model, two reduced-order Koopman-based control models have shorter computation times as compared to the the full-order Koopman-based control. Specifically, the computation times of the reduced-order KMPC and RKMPC are 44.82%, 44.55% faster than the full-order KMPC, respectively.

## 6 Conclusion

In this paper, we proposed a reduced-order Koopman-based robust predictive control approach. The Kalman-GSINDy algorithm was exploited to identify appropriate lifting functions for Koopman modeling. A POD-based reduced-order Koopman modeling approach was proposed, which can be used to construct accurate linear representations of general nonlinear processes while reducing the dimensionality of the resulting linear model compared to the traditional Koopman modeling. A reduced-order robust Koopman MPC design was formulated. A benchmark chemical process was introduced to illustrate the efficacy of the proposed framework. We also compared the performance of the proposed approach with two baselines in terms of tracking performance and computational efficiency. The proposed method can significantly reduce the computational time while providing comparable set-point tracking accuracy.

## Acknowledgment

This research is supported by Ministry of Education, Singapore, under its Academic Research Fund Tier 1 (RS15/21).

## References

- [1] P. Daoutidis, J. H. Lee, I. Harjunkski, S. Skogestad, M. Baldea, and C. Georgakis. Integrating operations and control: A perspective and roadmap for future research. *Computers & Chemical Engineering*, 115:179–184, 2018.
- [2] P. D. Christofides, R. Scattolini, D. Muñoz de la Peña, and J. Liu. Distributed model predictive control: A tutorial review and future research directions. *Computers & Chemical Engineering*, 51:21–41, 2013.



- [3] X. Yin and J. Liu. Subsystem decomposition of process networks for simultaneous distributed state estimation and control. *AIChE Journal*, 65(3):904–914, 2019.
- [4] P. Daoutidis, M. Zachar, and S. S. Jogwar. Sustainability and process control: A survey and perspective. *Journal of Process Control*, 44:184–206, 2016.
- [5] M. Ellis, J. Liu, and P. D. Christofides. Economic model predictive control. *Springer*, 5(7):65, 2017.
- [6] M. A. Henson. Nonlinear model predictive control: current status and future directions. *Computers & Chemical Engineering*, 23(2):187–202, 1998.
- [7] H. Chen and F. Allgöwer. A quasi-infinite horizon nonlinear model predictive control scheme with guaranteed stability. *Automatica*, 34(10):1205–1217, 1998.
- [8] M. Cannon. Efficient nonlinear model predictive control algorithms. *Annual Reviews in Control*, 28(2):229–237, 2004.
- [9] B. R. Maner, F. J. Doyle III, B. A. Ogunnaike, and R. K. Pearson. Nonlinear model predictive control of a simulated multivariable polymerization reactor using second-order volterra models. *Automatica*, 32(9):1285–1301, 1996.
- [10] A. Zheng. A computationally efficient nonlinear MPC algorithm. *Proceedings of the American Control Conference*, 1623–1627, 1997, Albuquerque, NM, USA.
- [11] S. Jain and F. Khorrami. Decentralized adaptive control of a class of large-scale interconnected nonlinear systems. *IEEE Transactions on Automatic Control*, 42(2):136–154, 1997.
- [12] J. Liu, D. Muñoz de la Peña, and P. D. Christofides. Distributed model predictive control of nonlinear process systems. *AIChE Journal*, 55(5):1171–1184, 2009.
- [13] B. O. Koopman. Hamiltonian systems and transformation in Hilbert space. *Proceedings of the National Academy of Sciences*, 17(5):315–318, 1931.
- [14] J. L. Proctor, S. L. Brunton, and J. N. Kutz. Generalizing Koopman theory to allow for inputs and control. *SIAM Journal on Applied Dynamical Systems*, 17(1):909–930, 2018.
- [15] M. Korda and I. Mezić. Linear predictors for nonlinear dynamical systems: Koopman operator meets model predictive control. *Automatica*, 93:149–160, 2018.

- [16] S. Das, S. Mustavee, S. Agarwal, and S. Hasan. Koopman-theoretic modeling of quasiperiodically driven systems: Example of signalized traffic corridor. *IEEE Transactions on Systems, Man, and Cybernetics: Systems*. In press, doi:10.1109/TSMC.2023.3253077, 2023.
- [17] S. L. Brunton, B. W. Brunton, J. L. Proctor, and J. N. Kutz. Koopman invariant subspaces and finite linear representations of nonlinear dynamical systems for control. *PloS one*, 11(2):1-19, 2016.
- [18] H. Arbabi, M. Korda, and I. Mezić. A data-driven Koopman model predictive control framework for nonlinear partial differential equations. *IEEE Conference on Decision and Control*, 6409–6414, 2018, Miami, FL, USA.
- [19] P. J. Schmid. Dynamic mode decomposition of numerical and experimental data. *Journal of Fluid Mechanics*, 656:5–28, 2010.
- [20] Y. Wang, Y. Yang, Y. Pu, and C. Manzie. Robust tracking model predictive control with Koopman operators. *IEEE Conference on Control Technology and Applications*, 1234–1239, 2022, Trieste, Italy.
- [21] S. H. Son, H. K. Choi, J. Moon, and J. S. I. Kwon. Hybrid Koopman model predictive control of nonlinear systems using multiple EDMD models: An application to a batch pulp digester with feed fluctuation. *Control Engineering Practice*, 118:104956, 2022.
- [22] A. Narasingam, and J. S. I. Kwon. Koopman Lyapunov-based model predictive control of nonlinear chemical process systems. *AIChE Journal*, 65(11):e16743, 2019.
- [23] S. H. Son, A. Narasingam, and J. S. I. Kwon. Development of offset-free Koopman Lyapunov-based model predictive control and mathematical analysis for zero steady-state offset condition considering influence of Lyapunov constraints on equilibrium point. *Journal of Process Control*, 118:26–36, 2020.
- [24] X. Zhang, W. Pan, R. Scattolini, S. Yu, and X. Xu. Robust tube-based model predictive control with Koopman operators. *Automatica*, 137:110114, 2022.
- [25] G. Pannocchia, and J. B. Rawlings. Disturbance models for offset-free model-predictive control. *AIChE Journal*, 49(2):426–437, 2003.

- [26] U. Maeder, F. Borrelli, and M. Morari. Linear offset-free model predictive control. *Automatica*, 45(10):2214–2222, 2009.
- [27] S. H. Son, H. K. Choi, and J. S. I. Kwon. Application of offset-free Koopman-based model predictive control to a batch pulp digester. *AIChE Journal*, 67(9):e17301, 2021.
- [28] S. H. Son, A. Narasingam, and J. S. I. Kwon. Handling plant-model mismatch in Koopman Lyapunov-based model predictive control via offset-free control framework. *arXiv preprint arXiv:2010.07239*, 2020.
- [29] B. Lusch, J. N. Kutz, and S. L. Brunton. Deep learning for universal linear embeddings of nonlinear dynamics. *Nature Communications*, 9(1):4950, 2018.
- [30] J. C. Schulze, D. T. Doncevic, and A. Mitsos. Identification of MIMO Wiener-type Koopman models for data-driven model reduction using deep learning. *Computers & Chemical Engineering*, 161:107781, 2022.
- [31] Y. Han, W. Hao, and U. Vaidya. Deep learning of Koopman representation for control. *IEEE Conference on Decision and Control*, 1890–1895, 2020, Jeju, South Korea.
- [32] E. Yeung, S. Kundu, and N. Hodas. Learning deep neural network representations for Koopman operators of nonlinear dynamical systems. *American Control Conference*, 4832–4839, 2019, Philadelphia, PA, USA.
- [33] A. Ahmed, E. A. del Rio-Chanona, and M. Mercangöz. Linearizing nonlinear dynamics using deep learning. *Computers & Chemical Engineering*, 170:108104, 2023.
- [34] S. L. Brunton, J. L. Proctor, and J. N. Kutz. Discovering governing equations from data by sparse identification of nonlinear dynamical systems. *Proceedings of the National Academy of Sciences*, 113(15):3932–3937, 2016.
- [35] U. Fasel, E. Kaiser, J. N. Kutz, B. W. Brunton, and S. L. Brunton. SINDy with control: A tutorial. *IEEE Conference on Decision and Control*, 16–21, 2021, Austin, TX, USA.
- [36] F. Abdullah and P. D. Christofides. Data-based modeling and control of nonlinear process systems using sparse identification: An overview of recent results. *Computers & Chemical Engineering*, 108247, 2023.

- [37] J. Wang, J. Moreira, Y. Cao, and B. Gopaluni. Time-variant digital twin modeling through the Kalman-generalized sparse identification of nonlinear dynamics. *American Control Conference*, 5217–5222, 2022, Atlanta, GA, USA.
- [38] Y. C. Liang, H. P. Lee, S. P. Lim, W. Z. Lin, K. H. Lee, and C. G. Wu. Proper orthogonal decomposition and its applications—Part I: Theory. *Journal of Sound and Vibration*, 252(3):527–544, 2002.
- [39] M. Rathinam and L. R. Petzold. A new look at proper orthogonal decomposition. *SIAM Journal on Numerical Analysis*, 41(5):1893–1925, 2003.
- [40] S. Liu, X. Yin, and J. Liu. State estimation of a carbon capture process through POD model reduction and neural network approximation. *arXiv preprint*, arXiv:2304.05514, 2023.
- [41] X. Yin and J. Liu. State estimation of wastewater treatment plants based on model approximation. *Computers & Chemical Engineering*, 111:79–91, 2018.
- [42] J. L. Lumley. The structure of inhomogeneous turbulent flows. *Atmospheric Turbulence and Radio Wave Propagation*, 166–178, 1967.
- [43] N. Aubry. On the hidden beauty of the proper orthogonal decomposition. *Theoretical and Computational Fluid Dynamics*, 2(5-6):339–352, 1991.
- [44] V. B. Nguyen, S. B. Q. Tran, S. A. Khan, J. Rong, and J. Lou. POD-DEIM model order reduction technique for model predictive control in continuous chemical processing. *Computers & Chemical Engineering*, 133:106638, 2020.
- [45] H. V. Ly and H. T. Tran. Modeling and control of physical processes using proper orthogonal decomposition. *Mathematical and Computer Modelling*, 33(1-3):223–236, 2001.
- [46] X. Zhang, M. Han, and X. Yin. Data-driven linear predictive control of nonlinear processes based on reduced-order Koopman operator. *IEEE International Conference on Systems, Man, and Cybernetics*, 2023, Honolulu, HI, USA.
- [47] A. Narasingam and J. S. I. Kwon. Application of Koopman operator for model-based control of fracture propagation and proppant transport in hydraulic fracturing operation. *Journal of Process Control*, 91:25–36, 2020.

- [48] M. O. Williams, M. S. Hemati, S. T. M. Dawson, I. G. Kevrekidis, and C. W. Rowley. Extending data-driven Koopman analysis to actuated systems. *IFAC-Papers OnLine*, 49(18):704–709, 2016.
- [49] M. O. Williams, I. G. Kevrekidis, and C. W. Rowley. A data-driven approximation of the Koopman operator: Extending dynamic mode decomposition. *Journal of Nonlinear Science*, 25:1307–1346, 2015.
- [50] P. Shah, M. Z. Sheriff, M. S. F. Bangi, C. Kravaris, J. S. I. Kwon, C. Botre, and J. Hirota. Deep neural network-based hybrid modeling and experimental validation for an industry-scale fermentation process: Identification of time-varying dependencies among parameters. *Chemical Engineering Journal*, 441:135643, 2022.
- [51] J. Li, M. Suvarna, L. Pan, Y. Zhao, and X. Wang. A hybrid data-driven and mechanistic modelling approach for hydrothermal gasification. *Applied Energy*, 304:117674, 2021.
- [52] G. E. Karniadakis, I. G. Kevrekidis, L. Lu, P. Perdikaris, S. Wang, and L. Yang. Physics-informed machine learning. *Nature Reviews Physics*, 3(6):422–440, 2021.
- [53] G. Wu, W. T. G. Yion, K. L. N. Q. Dang, and Z. Wu. Physics-informed machine learning for MPC: Application to a batch crystallization process. *Chemical Engineering Research and Design*, 192:556–569, 2023.
- [54] D. Q. Mayne, M. M. Seron, and S. V. Raković. Robust model predictive control of constrained linear systems with bounded disturbances. *Automatica*, 41(2):219–224, 2005.
- [55] J. Zhang and J. Liu. Distributed moving horizon state estimation for nonlinear systems with bounded uncertainties. *Journal of Process Control*, 23(9):1281–1295, 2013.
- [56] X. Li, S. Bo, Y. Qin, and X. Yin. Iterative distributed moving horizon estimation of linear systems with penalties on both system disturbances and noise. *Chemical Engineering Research and Design*, 194:878–893, 2023.